journal homepage: www.brodogradnja.fsb.hr

Brodogradnja

An International Journal of Naval Architecture and Ocean Engineering for Research and Development

An experimental investigation into the resistance characteristics of dimpled plates at high Reynolds numbers

Aras Çetinkaya, Uğur Oral Ünal*

Faculty of Naval Architecture and Ocean Engineering, Istanbul Technical University, Turkiye

ARTICLE INFO

Keywords:
Dimpled surfaces
Frictional drag reduction
Flat plate resistance
Cavitation tunnel

ABSTRACT

Over the past quarter-century, substantial research has been conducted on the potential of dimpled surfaces to passively reduce turbulent friction resistance. This potential is particularly intriguing in the context of external flows, particularly with applications in the transportation sector, such as maritime vessels, rail systems, and aerial vehicles. However, the literature presents conflicting findings and interpretations about the performance of the dimples and the underlying physical mechanisms of the flow. Furthermore, many of the studies do not address the requirements for assessing the efficiency regarding practical engineering, such as high Reynolds number flow and open boundary layer conditions. In this study, the effect of dimpled surfaces on resistance reduction was experimentally investigated. A specialized testing bed, capable of accommodating large test plates, was designed for use in a cavitation tunnel facility. This setup allowed for the achievement of a high Reynolds number range suitable for practical applications, while ensuring that external flow conditions were met. Critical parameters affecting resistance reduction performance such as coverage ratio and boundary layer thickness, were also examined. The resistance values obtained within a broad experimental matrix suggest that, under favourable conditions, dimpled surfaces can be highly effective in terms of energy efficiency. The insights and interpretations drawn from these findings are expected to provide valuable guidance for future research.

1. Introduction

In terms of environmental and economic impacts, low emissions and high fuel efficiency have gained significant importance, particularly over the last several decades. This situation encourages intensive research into drag-reduction methods for transportation vehicles exposed to fluid resistance. A substantial portion of the resistance caused by external flow is attributed to friction drag. Reducing the friction drag acting on objects moving within a fluid is crucial for maritime transport, which holds the largest share in global transportation. The methods examined for reducing friction drag can generally be categorized into active and passive approaches. Active methods require an energy input into the system, necessitating additional mechanisms to provide this energy. Although some studies have shown considerable effectiveness, the feasibility of applying

* Corresponding author.
E-mail address: cetinkayaar@itu.edu.tr

http://dx.doi.org/10.21278/76302
Submitted 18 November 2024; Received in revised form 10 March 2025; Accepted 27 March 2025
Available online 08 April 2025
ISSN 0007-215X; eISSN 1845-5859

these methods to vehicles poses challenges due to the required additional machinery. As an active method, a significant area of research in maritime transport is air lubrication systems, with recent studies [1-4] serving as examples in this field.

Passive methods are believed to be more suitable for application in vehicles. These methods include either coating applications related to chemistry and materials science, such as hydrophobic paints, or practices involving geometric structure modifications [5, 6] that pertain to fluid mechanics and engineering applications. Although one of the first successful applications in geometric design, the effects of riblets on fluid mechanics are not yet fully understood; however, the primary goal of these applications is to increase the vortical structures and turbulence intensity along the flow direction axis, which in turn enhances the height of the viscous sublayer. Consequently, it is thought that the momentum transfer between layers can be shifted significantly from the flow direction to other directions, thus reducing the transition of vortices to the outer boundary layer. This method is believed to decrease the Reynolds stresses along the flow direction on the fluid's surface and reduce the friction drag in the flow direction [7-10]. Although studies have reported a significant reduction in resistance (5-15%) via riblets, it has been noted that their practical applicability, particularly for the external surfaces of vehicles, is limited. Contributing factors include the additional weight added to these surfaces and increased maintenance and operational costs due to issues such as fouling and wear [11].

An alternative passive application, dimpled surfaces, and prominent frictional drag-reduction capabilities under turbulent flow conditions have been significant focuses of research for several decades. Following the discovery of their potential to enhance heat transfer [12, 13], it has become evident that interactions among dimples can induce spanwise flow components and fluctuations. These effects can passively achieve drag reduction, comparable to active drag-reduction techniques such as oscillating walls [14-16] or the application of electromagnets to generate Lorentz forces in conducting fluid flows) [17, 18].

Most existing studies have primarily investigated circular, symmetrical dimple structures. However, even within this simple geometry, defining the flow mechanisms and determining the optimal dimple parameters for significant drag reduction remains challenging. Key parameters include the dimple depth-to-diameter ratio (d/D), Reynolds number, coverage ratio (f_a), which refers to the ratio of the projected area of the dimples to the total flat surface area without dimples, dimple arrangement pattern (flow-aligned or staggered), boundary layer thickness relative to the dimple diameter (δ/D or H/D for channel flows), and geometric shape of the dimples (circular, elliptical, drop-like, diamond, etc.). The large number of parameters affecting the flow structure naturally complicates the design of effective dimple geometries.

In their studies, Zhao et al. [19] examined dimple depth-to-diameter ratios of 4%, 20%, and 50%, focusing on the effects of sharp and rounded edges in water channels with conditions of $Re_D < 4 \times 10^4$, $H/D = 0.5$, $f_a = 0.47$, and a staggered arrangement. Their visualization with dye injection in a water tunnel revealed that $d/D = 4$ did not cause flow separation at higher Reynolds numbers, whereas $d/D = 20$ and 50 resulted in chaotic horseshoe and vertical vortices, described as "tornado-like" by some researchers, e.g., [20]. They found that rounded edges performed better than sharp edges, with $d/D = 4\%$ dimples reducing friction by 2% to 15%, depending on the Reynolds number.

Lienhart et al. [21] conducted experiments in both channel flows and open boundary layers, as well as direct numerical simulations (DNS), with dimples arranged in a staggered pattern at $f_a = 0.225$ and $d/D = 5\%$, up to $Re_D = 24{,}325$. Their results indicate that although dimples can reduce frictional drag, they often increase form drag, thus diminishing the overall reduction in drag.

Veldhuis and Velvoort [22] explored dimpled plates at $f_a = 0.6$ in both staggered and flow-aligned arrangements up to $Re_D \approx 7 \times 10^4$ in a wind tunnel. They tested various depth-to-diameter ratios between 1.14% and 11.67%. Their findings show that the flow-aligned pattern exhibited negligible drag reduction, whereas the staggered pattern, particularly with shallow dimples, performed better. For $d/D = 1.67$, a drag reduction of 5% was observed at high Reynolds numbers and 13% at $Re_D \approx 12{,}600$. They also noted that large eddy simulations (LESs) produced higher drag magnitudes than those observed during the experiments.

Tay et al. [23] conducted an experimental study in channel flow conditions with Reynolds numbers ranging from 25,000 to 18,500, investigating two different d/D ratios (1.5% and 5%) in a staggered pattern.

They compared two coverage ratios, f_a = 0.4 and 0.9, for deeper dimples. Their results indicate that with a high coverage ratio of 0.9, the shallower dimples reduced the drag force by approximately 2% across the Reynolds range, whereas deeper dimples increased the drag at lower Reynolds numbers and reduced it slightly more (about 3%) at higher Reynolds numbers. For f_a = 0.4, the trends were similar, but the percentages of drag increase were smaller at lower Reynolds numbers, and reduction occurred at higher Reynolds numbers. They also examined spanwise inductions on the near-wall velocity field and fluctuations in streamlines.

Van Nesselrooij et al. [24] performed extensive investigations into the effects of dimple depth-to-diameter ratio (d/D), coverage ratio (f_a), arrangement pattern, and boundary layer thickness on drag reduction in open boundary-layer conditions up to Re_D = 40,000 using a wind tunnel. They found that staggered patterns were more effective than flow-aligned patterns; lower coverage ratios (f_a = 0.33) were preferable to higher ratios (f_a = 0.9), and shallower dimples (d/D = 2.5%) were more advantageous than deeper ones (d/D = 5%). They noted that thicker boundary layers weakened the drag reduction trend with the Reynolds number, limiting the maximum drag reduction to 4%. Their visual investigations using PIV (particle image velocimetry) and fluorescent oil applications provide valuable insight into the flow mechanisms underlying drag reduction. Spalart et al. [25] carried out experiments using the NASA Langley 7 facility and almost identical dimple configurations (d/D = 2.5%, f_a = 0.29, δ/D =0.75, $Re_D \approx$ 40,000), along with DNS simulations for corroboration. However, their results were controversial, showing a 1% drag increase rather than the drag reduction claimed in [24]. In addition, Van Campenhout et al. [26] scrutinized the replicability of the potential drag-reducing conditions; however, with their improved setup for measuring pressure, their findings support the results reported in [25].

Tay et al. [27] conducted numerical detached eddy simulations (DES) at Reynolds numbers between 3300 and 15000, validating their experimental results with staggered dimples of d/D = 5% and 1.5%. They analyzed pressure fields, skin friction ratios, transverse velocities, stream-wise velocity trails, and fluctuations, emphasizing the balance between frictional gains and pressure drag deficits to achieve a reduction in the overall drag. Their examination of the energy budget reveals that the dimpled cases with increased drag exhibited higher peaks in various terms compared to flat plates, whereas the cases with reduced drag had lower or comparable peaks. They noted that DES is effective for simulating large-scale flow features, particularly flow separations, but less accurate in predicting skin friction.

Recent studies have explored geometric improvements to enhance drag characteristics, such as implementing tear-drop, diamond, or elliptical dimples or altering the axisymmetry of circular dimples by shifting the deepest point [28, 29]. These studies found that shifting the deepest point of the circular dimples approximately 0.1 D downstream or using elliptical- or diamond-shaped dimples reduced the upstream slope and improved the likelihood of avoiding flow separations inside the dimples.

İlter et al. [30] performed a large eddy simulation (LES) study on flow-aligned circular dimple arrangements under various d/D and Re_D conditions with a fixed bulk velocity flow and maximum coverage ratio. They also investigated diamond-shaped dimples to assess potential advantages over circular ones, offering detailed information and explanations about flow field and kinetic energy budget.

Many low-speed merchant ships, such as tankers, bulk carriers, and container ships, exhibit significant skin friction components as a percentage of their total resistance. These vessels typically feature long, flat surfaces with parallel hulls and keels, which are suitable for the implementation of dimples. However, to effectively utilize dimples on such vessels, their performance must be well understood and predicted at a high Reynolds number range. The vessels in question generally operate at cruising speeds between 9 and 20 knots, corresponding to Reynolds numbers of approximately $4\times10^5 < Re_D < 1\times10^6$ for dimples with a diameter of 100 mm. The existing literature includes very few studies addressing this Reynolds number range. As an exception, İlter et al. [31] conducted high-speed, fully turbulent flow channel experiments with circular dimple arrangements in a flow-aligned pattern and at f_a = 0.9 at Reynolds numbers ranging from 6×10^5 to 1.2×10^6. Their drag estimates based on pressure drop measurements show that the dimples with a diameter of 60 mm and diameter-to-depth ratio of 3% achieved significant drag reductions of up to 26.8%. Contrary to many previous studies, they found that the flow-aligned pattern was more effective than the staggered configuration,

particularly in cases with a high coverage ratio (f_a > 0.85). This study, however, was constrained by a fixed boundary layer thickness, a limitation inherent to the channel flow conditions.

Another important issue still under consideration is the determination of the optimal coverage ratio of the dimples. Some researchers argue that drag reduction can only be achieved with coverage ratios exceeding 70% [23, 32], whereas others suggest that the optimal coverage ratio should be around 35-60% [22, 24]. Moreover, most studies have been conducted under channel flow conditions, which may limit the development of the boundary layer, as encountered in full-scale flow scenarios.

To address the critical aspects discussed above, in this study, an experimental evaluation of the frictional resistance reduction potential of the dimpled surface was performed using large test plates in the cavitation tunnel at Istanbul Technical University. A high Reynolds number range suitable for practical applications in high-speed rail transport and, more specifically, in maritime commercial transportation was adopted. The dimpled plates had various coverage ratios in a staggered pattern at four different Reynolds numbers, and they were investigated with direct resistance measurement under open boundary-layer conditions by applying two different boundary-layer thicknesses for each incoming flow speed.

This study sheds significant light on the applicability of dimpled surfaces for real-life situations. To the best of the authors' knowledge, this work presents the first experimental investigation of dimpled structures involving large plates fitted in a water tunnel, allowing for direct resistance measurements in outer flow conditions at high Reynolds numbers.

2. Experimental Setup

2.1 Water tunnel facility and testing bed

The experiments were conducted in Istanbul Technical University's Cavitation Tunnel (ITUKAT). ITUKAT is a closed-circuit tunnel, which has a test section of 5.5×1.5×1.2 m. The tunnel contains 700 tons of water that circulates via a 1 MW electric motor driving a five-bladed impeller. The maximum flow speed in the test section is 16.5 m/s. The turbulence intensity inside the test section is less than 1% in all directions.

For accurate resistance measurements, a large testing bed was designed and manufactured using steel material. The details of the testing bed are shown in Figure 1. The testing bed consisted of the following two main parts: a fixed carriage and a sliding frame that housed the test plates. Plexiglas material was used for the flat and dimpled plates, which were framed with 10 mm thick stainless-steel beams bolted together. The frame was vertically placed at the center of the testing bed and allowed to move freely in the flow direction by means of several rollers. The testing bed was constructed from five pieces, which were connected to each other, as well as the upper hatch and bottom wall, by several rods to ensure stability and easy installation inside the test section of the cavitation tunnel. A schematic view of the measurement system is presented in Figure 2.

The test plates were made of Plexiglas and were machined on both sides with dimensions of 2600×900×150 mm. They were encircled by a 10 mm thick stainless-steel beam forming a frame, which was tightened by vertical rods to dampen potential vibrational disturbances. The total length and height of the double-sided test plates were 2620 mm and 920 mm, respectively. The forward structure of the testing bed had a length of 1170 mm, which helped generate a turbulent boundary layer toward the test plates. A 2 mm wide gap was left between the test frame and the bed, which was sufficient to allow the frame to transfer the load to a uniaxial load cell.

2.2 Geometry of dimples

According to the literature review, it is evident that the dimple depth-to-diameter ratio should be less than 5% (e.g., [21-24]). It is also important that these dimples do not compromise the vessel's structural integrity or significantly increase its weight. On the other hand, very shallow dimples (i.e., d/D<2%) may pose challenges in precise manufacturing and could become ineffective over time due to fouling in full-scale applications. Consequently, a depth ratio of d/D= 3% was selected in the current study. A spherical geometry was implemented for the dimples on all plates. The dimples were 100 mm in diameter, with a depth of 3 mm,

radius of 1 mm, and edge smoothing, as shown in Figure 3. The machining tolerance for the dimple geometry was ± 0.3 mm.

Four different arrangements were applied, which varied in the coverage ratio (f_a), referring to the ratio of the projected area of the dimples to the plate area on which the pattern was implemented, in a staggered formation. The dimpled surfaces were labeled according to their coverage ratio, from high to low, as DD1, DD2, DD3, and DD4. The arrangement of the dimpled structures is shown in Figure 4. The centers of the dimples were arranged in an equilateral triangle pattern, as shown in Figure 5. The applied dimple configurations are listed in Table 1.

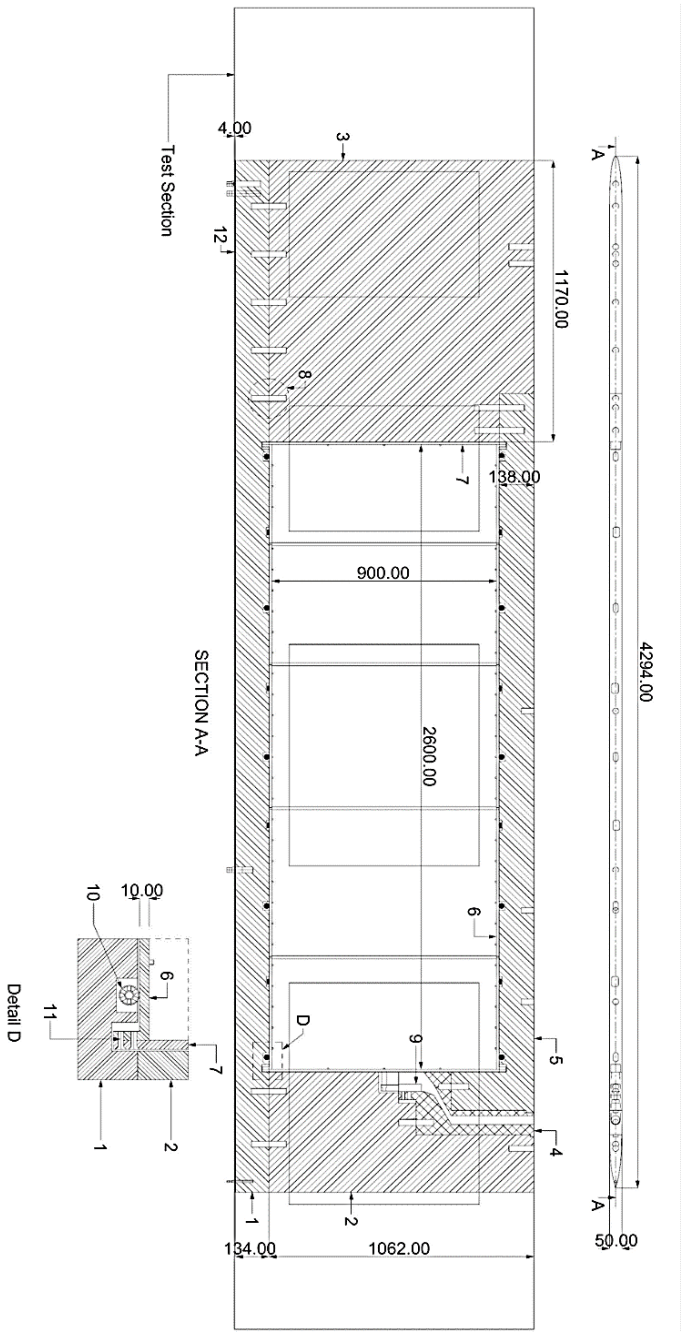

Fig. 1 Construction details of the testing bed. (1) Floor structure; (2) rear structure; (3) fore structure; (4) load-cell case; (5) ceiling structure; (6) upper and lower beams of the test-plate frames; (7) front and rear beams of the test-plate frames; (8) connection rods; (9); load cell; (10) rollers; (11) frame bolts; (12) bottom rubber "NBR 70 shore"

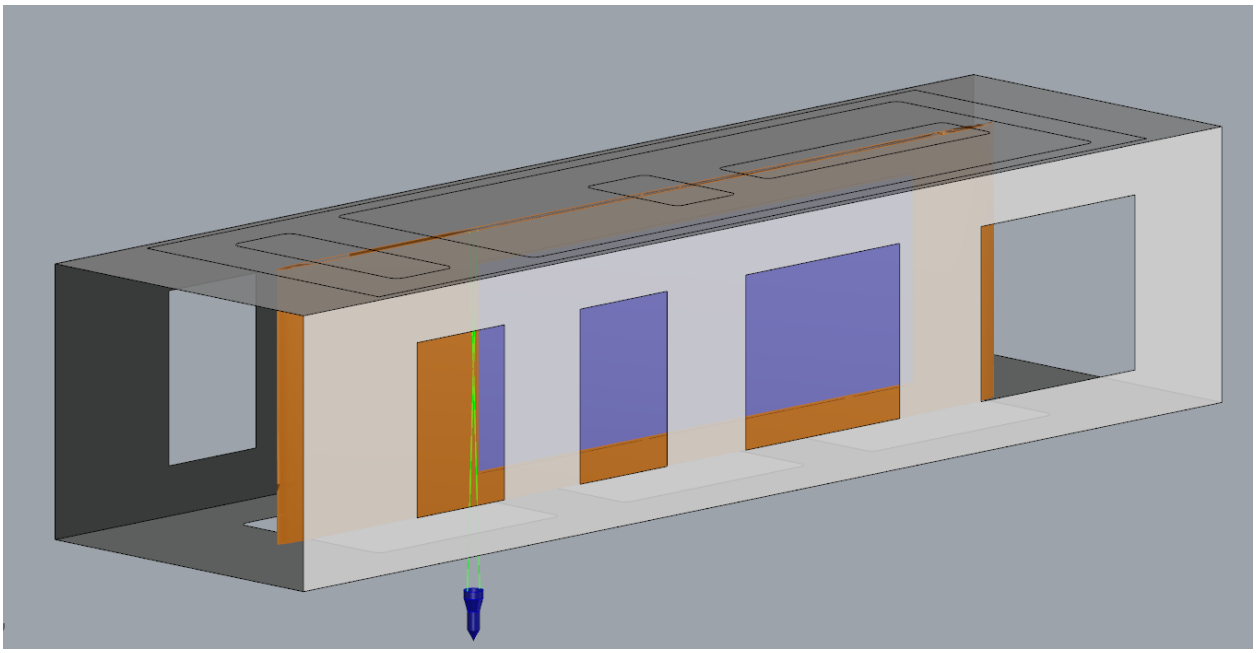

Fig. 2 Schematic view of the measurement system

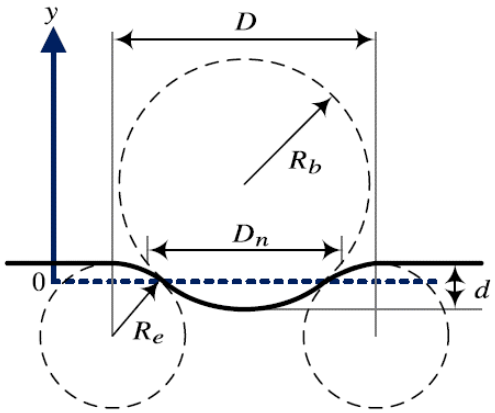

Fig. 3 Geometric parameters of a single spherical dimple (R_e = 1 mm; D_n = 99.761 mm; R_b = 417.167 mm; D = 100 mm; d = 3 mm)

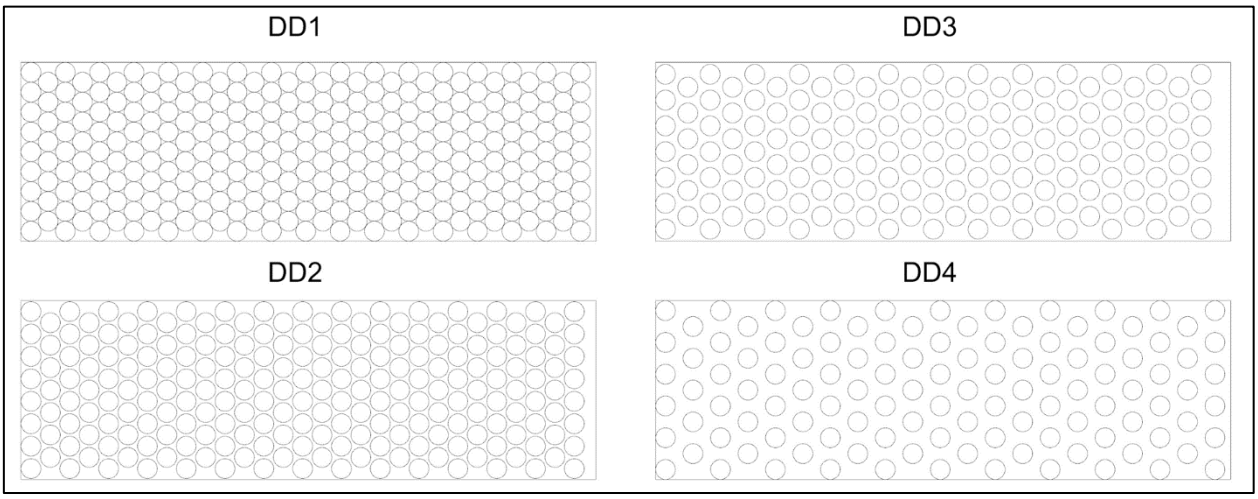

Fig. 4 Arrangements of test plates with different coverage ratios

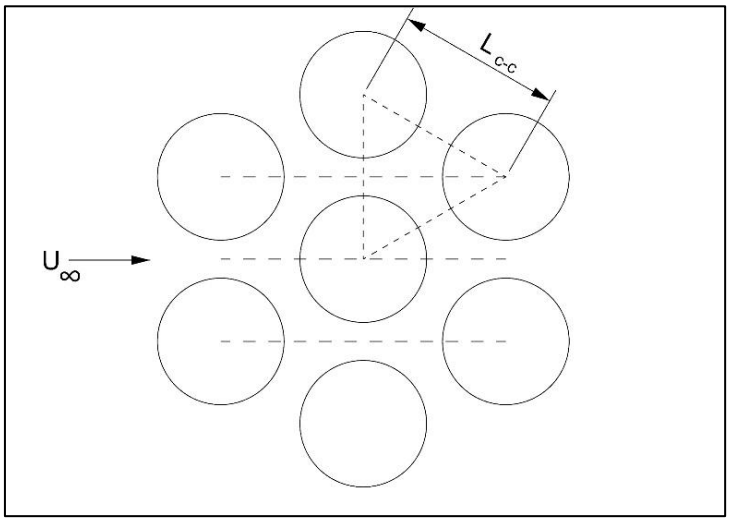

Fig. 5 The $L_{c\text{-}c}$ values for DD1, DD2, DD3 and DD4 are 100, 113, 130 and 160 mm respectively

Table 1 Distances between dimple centers and the coverage ratios of dimple arrangements on plates

Plate Arrangements		
Plates	$L_{c\text{-}c}$ (mm)	f_a
DD1	100	0.907
DD2	113	0.710
DD3	130	0.537
DD4	160	0.354

2.3 Experiments

The experiments were carried out at four different freestream velocities—4, 6, 8, and 10 m/s—which were represented as sub-indices 1 to 4 for the related parameter. An additional set of experiments was also conducted with a thicker boundary layer [33], hastened by applying 40-grit sandpaper over the 970 mm upstream part of the fore structure. The boundary layers under smooth fore structure conditions and rough conditions were labeled BL0 and BL1, respectively. The test matrix of the experiments and related parameters are listed in Table 2.

A two-dimensional DANTEC laser Doppler velocimetry (LDV) system was used for measuring the boundary layer thickness. The LDV system consisted of two separate 1 W laser light sources, used for the generation of the green (514.5 nm) and blue (488 nm) laser beams; a beam separator; fiber-optic probe; signal processor; traverse controller; and three-axis traverse. The system was controlled by a PC with the aid of dedicated software. The 40 MHz Bragg cell removed the directional ambiguity. The system operated a 60 mm probe with a beam spacing of 38 mm. Polyamide particles with a particle size of 20 μm were used as seeding material. The probe volume diameters were 143 μm and 151 μm in the streamwise and transverse directions, respectively. The probe was located under the test section where the beams propagated parallel to the test plate through the bottom windows (see Figure 2), which meant one of the secondary beams was blocked by the testing bed, and only the streamwise velocity component inside the boundary layer could be measured using the green light source. The streamwise velocity within the outer boundary layer was scanned at 0.25 mm intervals.

The boundary layer thickness was determined as the perpendicular distance between the surface and the location, where the streamwise velocity reached 99% of V_∞. Measurement took place at the x-position of 5 mm ahead of the end of the front structure and z position where the corresponding the vertical symmetry centerline. For each specific point, the data acquisition's duration was kept constant at 60 seconds, resulting in a sampling data rate between 100 and 350, with a standard error of < 0.63%.

Force measurements were acquired using an Esit SBS-200-C3 load cell. The analog data were digitalized using a HBM QuantumX MX84OBf analog–digital converter. The final signal processing was performed with Catman software. Each measurement represents 18,000 data points at 300 Hz over a 60-second duration; after every 3 seconds, the mean value stabilizes within a range of ± 0.5 N for approximately 90 seconds to reach an ultimate mean value.

The maximum of the standard errors calculated among the individual force signals was 2.3%. During the experiments, the temperature of the water in the cavitation tunnel varied around 20 ± 1°C. Hence, the specific error due to the varying kinematic viscosities was 0.35%. To assess the uncertainty of the precision in the experiments, both FP conditions with the two boundary layer thicknesses considered were repeated 7 times, whereas the other cases were repeated 4 times for all freestream velocities. For the FP measurements, the test plate was removed and reinstalled two times after the second and fourth runs. In other cases, the removal and reinstallation process was applied only one time after the second run. The overall uncertainty with 95% confidence bounds was found to be lower than 4.1%.

Table 2 Details on the experimental parameters

V_∞ (m/s)	0.99*V_∞	Re_D	δ_0 (mm)	δ_0/D	δ_1 (mm)	δ_1/D	δ_1/δ_0
4	3.96	~4×10^5	13.0	0.130	29.0	0.290	2.23
6	5.94	~6×10^5	12.8	0.128	28.5	0.285	2.24
8	7.92	~8×10^5	12.3	0.123	24.5	0.245	2.00
10	9.90	~1×10^6	11.8	0.118	23.8	0.238	2.02

3. Determination of Drag Components on the Experimental Setup

To identify the resistance sources originating from the structure of the designed measurement system rather than from the test plates themselves, a CFD study comprising two stages was conducted for the flat plate (FP) cases.

In the first stage, 2D simulations were performed on a horizontal (X–Y) plane section passing through the vertical center of the experimental setup. The gaps around the test plate were closed to simulate a flow regime akin to that of a flat plate. The results of the 2D simulations, conducted using an ideally selected mesh structure following a mesh independence study, were validated using the Prandtl–Schlichting formula (Equation (1)) for the frictional coefficient of the flat plates [34].

$$C_f = 0.455\left(\log\frac{V_\infty x}{\nu}\right)^{-2.58} \tag{1}$$

In the second stage, 3D simulations were performed, with the mesh structures generated following an additional mesh dependency study. In this supplementary study, the resolution was solely adjusted along the vertical (Z) axis, using the previously verified and validated 2D mesh grids. Additionally, a refined mesh was specifically applied to the gaps between the experimental setup and the test plates to enhance accuracy. The boundary-layer thickness and drag measurements from the FP experiments were then compared with the results from the 3D simulations.

For both the numerical analyses and theoretical calculations, the fluid's conditional parameters were based on measurements from the cavitation tunnel, which provided the following values during the experiments: density (ρ_w) = 998.8 kg/m³, kinematic viscosity (ν_w) = 1.0034×10^{-6} m²/s, and an average temperature (T_w) = 20°C. Details of the numerical simulations and the associated uncertainties are discussed in the following sections.

3.1 Computational Procedure

For the fully turbulent boundary layer analyses, steady, incompressible RANS equations were solved for the smooth, flat plate validation study. To calculate the turbulence field and, hence, model the Reynolds stresses, which arise in RANS equations after the averaging operation as additional unknowns, the SST k-ω

turbulence model [35], which is based on the Boussinesq hypothesis [36], was used. Turbulence transport equations were solved by the finite volume technique with a segregated algorithm [37, 38]. For the pressure-velocity coupling, a standard pressure-correction procedure, SIMPLE (semi-implicit method for pressure-linked equations), was applied [39]. The second-order upwind scheme was used to discretize the convective acceleration terms, whereas the viscous terms were dealt with using the second-order central difference scheme [40]. In each case, the iterations were run until the scaled residual of continuity dropped to a level of 10^{-6}.

3.1.1 Computational mesh and verification study for 2D cases.

The 2D solution domains in the X–Y plane were defined by the unit height and half of the width of the test section, utilizing symmetry around the central vertical plane. The inlet and outlet boundaries were positioned 1500 mm upstream and 3000 mm downstream of the test section, respectively. The tunnel side wall was aligned parallel to the incoming flow, featuring a slip wall that diverged by 26 mm toward the downstream to minimize boundary-layer disturbances and maintain uniform flow within the test section. A velocity inlet boundary condition was applied at the upstream boundary, with the turbulence intensity set to 1%, as measured in the cavitation tunnel. For the outlet boundary, a Neumann-type boundary condition was employed. The non-dimensional wall distance (y^+) of the first adjacent cell was maintained at approximately 3, and during the post-processing stage, the y^+ distribution was evaluated to confirm that the majority of values did not exceed 5, indicating that almost all first adjacent cells remained within the viscous sublayer. This approach ensures that the boundary layer is fully resolved down to the wall without using logarithmic wall functions. The growth rate near the wall region was set to 1.1 for wall treatment purposes.

A mesh dependence study was conducted using an unstructured mesh comprising tetrahedral and hexahedral cells, with three different resolutions under a constant incoming flow velocity of 8 m/s. The numerical discretization error was quantified using the Grid Convergence Index (GCI) method, as described in [41]. Upon selecting the optimal mesh resolution, additional mesh grids corresponding to varying incoming velocities were generated, maintaining a constant aspect ratio for the first adjacent cell and applying uniform length scales across all boundaries. Table 3 presents the GCI results for the 2D mesh structures. In the table, the average cell area (A) was calculated by dividing the total area of the 2D domain by the cell count, and the grid size (h) implies a square root of A, which represents the average length scale of the cells. The *GCI* value indicating the discretization uncertainty for the drag force, using a medium-resolution mesh, was determined to be 0.07%, which was considered sufficient for the remainder of the study. A detailed view of the medium-resolution mesh used for the 2D simulations is shown in Figure 6.

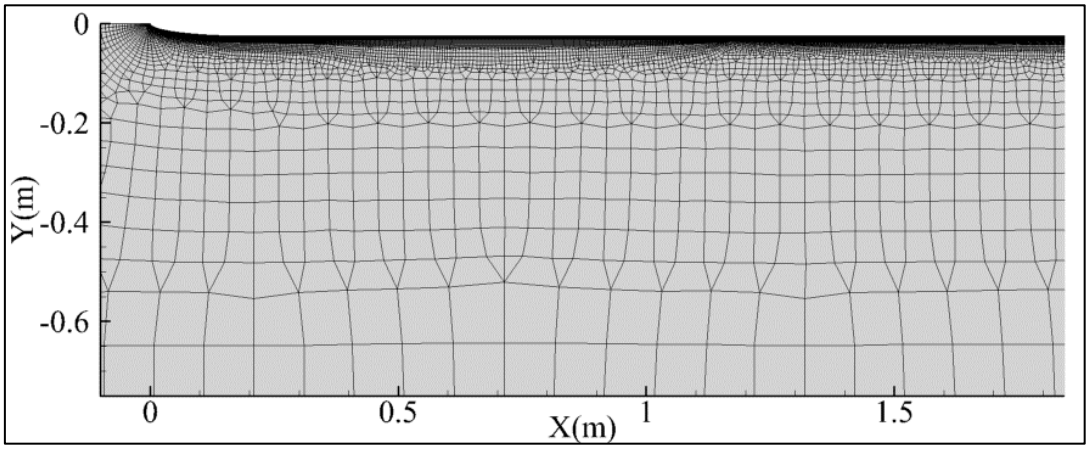

Fig. 6 A view of the medium-resolution mesh used in the 2D simulations

Table 3 Two-dimensional grid convergence study

Cell Count	Coarse (3)	78,323
	Medium (2)	155,303
	Fine (1)	355,094
Average Cell Area	A_3	103.998
	A_2	52.448
	A_1	22.938
Grid Size	h_3	10.198
	h_2	7.242
	h_1	4.789
Refinement Factor	r_{32}	1.408
	r_{21}	1.512
Drag (N)	Φ_3	196.7
	Φ_2	197.9
	Φ_1	198.2
Approximate Relative Error	e_{a_32}	0.0060
	e_{a_21}	0.0018
Convergence Index	GCI_{32} (%)	0.24
	GCI_{21} (%)	0.07

3.1.2 Computational mesh and verification study for 3D cases.

The 3D solution domain was defined as a quarter of the test section, in accordance with the symmetry of the experimental system along the central vertical and central horizontal planes. The regions with gaps between the testing bed and the test plate were also refined, and an additional mesh dependency study was performed by varying the resolution exclusively in the vertical direction. In this case, the previously selected 2D mesh was retained and extruded along the Z-axis with three different resolutions. The results of the corresponding GCI study are presented in Table 4. In the table, the average cell volume (V) was obtained by dividing the total volume of the 3D domain by the cell count, and the grid size (h) represents the cubic root of V. The table indicates that the medium-resolution mesh topology was sufficiently refined for further analysis. Figure 7 illustrates the selected medium-resolution mesh along the Z-axis, which defines the third dimension of the 3D mesh on the wall surface.

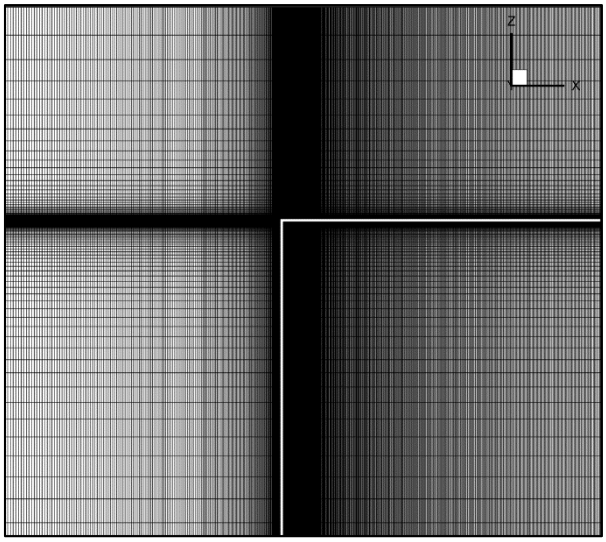

Fig. 7 X-Z plane view of the medium-resolution mesh used in 3D simulations

Table 4 Three-dimensional grid convergence study

Cell Count	Coarse (3)	22,655,115
	Medium (2)	43,678,770
	Fine (1)	77,894,230
Average Cell Volume	V_3	215.731
	V_2	111.971
	V_1	62.744
Grid Size	h_3	5.997
	h_2	4.820
	h_1	3.974
Refinement Factor	r_{32}	1.244
	r_{21}	1.213
Drag (N)	Φ_3	102.1
	Φ_2	106.2
	Φ_1	107.0
Approximate Relative Error	e_{a_32}	0.0380
	e_{a_21}	0.0076
Convergence Index	GCI_{32} (%)	1.44
	GCI_{21} (%)	0.29

The discrepancy between the drag values in Table 3 and Table 5 arises because of the differing domains of the 2D and 3D simulations. The 3D simulations encompass only the upper left portion of the experimental setup, extending along the upper wall of the tunnel's test section and the mid-plane (symmetry plane along the Z-axis). In contrast, the 2D simulations represent the drag values for a plate with a unit height (1 m) of the left part. The 3D simulations correspond to the drag values for half the height of the actual plate used in the experiments (0.46 m).

3.2 Validation of Drag Results and Determination of Drag Caused by the Gaps.

To validate the 2D simulations, the semi-empirical formula of Prandtl–Schlichting was applied to calculate the resistance of the testing plate. This calculation involved subtracting the resistance of the front structure of the testing bed from the total combined resistance of the front structure and the testing plate under condition BL0. The maximum difference in resistance was found to be 5.1 % at an incoming velocity of 4 m/s, which decreases to 1.5 % as the incoming velocity increases to 10 m/s, which is considered reasonable and sufficiently accurate. The 3D simulations, in this context, demonstrated even better agreement with the experimental results, with a maximum difference of 1.75 %. A comparison of the results for the empirical and 2D numerical drag forces, along with the 3D numerical and experimental results for the flat plate under BL0 conditions, is presented in Table 5.

Table 5 Drag force validation results of the simulations and experiments for the flat plate under condition BL0

		Drag without Gaps (N)			Actual Plate Drag with Gaps (N)		
V_∞(m/s)	Re_D	Prandtl-Schlichting	CFD-2D	$\varepsilon_{PS\text{-}CFD}$%	EFD	CFD-3D	$\varepsilon_{EFD\text{-}CFD}$%
4	3.99E+05	98	103	5.1	114	116	1.8
6	5.98E+05	209	215	2.9	242	243	0.4
8	7.97E+05	356	364	2.3	423	425	0.5
10	9.97E+05	539	547	1.5	629	630	0.2

For the validation of the experiments conducted under condition BL1 with a thicker boundary layer, an indirect method was employed. The RANS equations alone are insufficient to accurately simulate the effects

of the roughness induced by the sandpaper. Therefore, the required additional length of the smooth-surfaced front structure was determined by identifying the point at which the boundary layer thickness matched that measured by LDV at the trailing edge of the front plate in the initial 2D, smooth-surfaced simulation. Subsequently, additional 2D and 3D meshes were generated with an extended front structure to replicate the same boundary layer thickness developed in the experimental setup after the application of sandpaper, while maintaining identical mesh resolution parameters for the extended section. A comparison of the empirical and numerical results for the flat plate under condition BL1 is presented in Table 6. As shown in the table, the results are in close agreement and considered satisfactory for validating the experimental tests. The additional drag forces resulting from the gaps between the test plate and the setup structure are also provided in Table 7. The actual y^+ values obtained from each 2D and 3D simulation conducted under BL0 and BL1 conditions are also presented in Table 8. The values in the table indicate that the boundary layer was fully resolved down to the wall surface.

Table 6 Drag force validation results of the simulations and experiments for the flat plate under condition BL1

		Drag without Gaps (N)			Actual Plate Drag with Gaps (N)		
V_∞ (m/s)	Re_D	Prandtl–Schlichting	CFD-2D	$\varepsilon_{PS\text{-}CFD}$%	EFD	CFD-3D	$\varepsilon_{EFD\text{-}CFD}$%
4	3.99E+05	90	94	4.4	102	105	2.9
6	5.98E+05	191	199	4.2	223	226	1.4
8	7.97E+05	331	341	3.1	395	397	0.5
10	9.97E+05	502	520	3.6	582	591	1.6

Table 7 Increase in the drag force due to the gaps between the test plate and test frame

	V_∞ (m/s)	Drag without Gaps (N)	Drag with Gaps (N)	Gap Drag (N)
BL0	4	103	116	13
	6	215	243	28
	8	364	425	61
	10	547	630	83
BL1	4	94	105	11
	6	199	226	27
	8	341	397	56
	10	520	591	71

Table 8 Average and maximum y^+ values obtained from 2D and 3D simulations

		BL0		BL1	
	V_∞ (m/s)	y^+ (average)	y^+(max)	y^+ (average)	y^+(max)
2D	4	2.6	3.6	2.5	3.5
	6	2.9	3.7	2.7	3.5
	8	3.2	4.0	3.0	3.8
	10	3.6	4.3	3.5	4.3
3D	4	2.8	4.3	2.7	4.2
	6	3.2	4.7	3.0	4.5
	8	3.6	5.0	3.2	4.9
	10	3.7	5.0	3.5	5.0

3.3 Boundary Layer Comparisons

The comparison of boundary layer thickness results from the 3D simulations with gaps and the measurements conducted for the flat plate (FP) is provided in Table 9 for the upstream region and in Table 10 for the downstream region of the test plate. The tables indicate that the results are in good agreement, with the differences in thickness values ranging between 4% for BL0 and 8% for BL1.

Table 9 Boundary layer thicknesses at a position 5 mm forward of the trailing edge of the front structure

V_∞ (m/s)	0.99*V_∞	BL0-CFD (mm)	BL0-EFD (mm)	BL1-CFD (mm)	BL1-EFD (mm)
4	3.96	13.1	13.0	27.8	29.0
6	5.94	12.3	12.8	27.3	28.5
8	7.92	11.8	12.3	24.1	24.5
10	9.90	11.7	11.8	23.5	23.8

Table 10 Boundary layer thicknesses at a position 5 mm forward of the trailing edge of the test plate frame

V_∞ (m/s)	0.99*V_∞	BL0-CFD (mm)	BL0-EFD (mm)	BL1-CFD (mm)	BL1-EFD (mm)
4	3.96	34.3	34.5	46.6	47.5
6	5.94	32.6	33.3	44.5	45.8
8	7.92	31.3	31.8	40.9	43.3
10	9.90	30.2	31.0	40.0	41.8

4. Results and Discussion

The mean drag forces measured for conditions BL0 and BL1 are detailed in Tables 11 and 12, respectively. These tables include the additional pressure drag forces attributed to the gaps between the test plates and the stationary testing bed. To accurately assess the effect of the dimpled surfaces compared to a flat plate, the additional drag forces determined with the 2D and 3D numerical analyses were subtracted from the original measurements. The magnitudes of these subtracted forces are provided in the preceding chapter on the numerical validation. The corrected drag values and their comparisons for conditions BL0 and BL1 are presented in Tables 13 and 14, respectively.

Table 11 Measured drag force values under condition BL0 condition for the different plates (values are in N)

V_∞(m/s)	Re_D*10^{-5}	FP	DD1	DD2	DD3	DD4
4	3.99	114.3	113.8	111.3	112.0	112.8
6	5.98	241.6	241.0	233.8	232.5	236.5
8	7.97	423.4	426.0	408.5	387.3	410.3
10	9.97	629.0	654.8	615.3	535.8	596.8

Table 12 Measured drag force values under condition BL1 condition for the different plates (values are in N)

V_∞(m/s)	Re_D*10^{-5}	FP	DD1	DD2	DD3	DD4
4	3.99	102.3	108.0	105.0	100.8	101.3
6	5.98	222.9	234.8	228.5	216.5	219.5
8	7.97	394.6	412.3	403.3	365.5	386.3
10	9.97	582.3	605.0	590.3	503.0	558.3

Table 13 Corrected drag force and coefficient values under condition BL0 condition for the different plates

	$Re_D \times 10^{-5}$	3.99	5.98	7.97	9.97
FP	Drag Force (N)	101.3	213.6	362.4	546.0
	$C_D \times 10^3$	5.259	4.928	4.704	4.536
DD1	Drag Force (N)	100.8	213.0	365.0	571.8
	$C_D \times 10^3$	5.231	4.915	4.788	4.750
	ΔC_D%	-0.5	-0.3	0.7	4.7
DD2	Drag Force (N)	98.3	205.8	347.5	532.3
	$C_D \times 10^3$	5.101	4.748	4.537	4.422
	ΔC_D%	-3.00	-3.7	-4.12	-2.5
DD3	Drag Force (N)	99.0	204.5	326.3	452.8
	$C_D \times 10^3$	5.140	4.719	4.261	3.761
	ΔC_D%	-2.3	-4.3	-10.0	-17.1
DD4	Drag Force (N)	99.8	208.5	349.3	513.8
	$C_D \times 10^3$	5.179	4.811	4.559	4.268
	ΔC_D%	-1.5	-2.4	-3.6	-5.9

Table 14 Corrected drag force and coefficient values under condition BL1 condition for the different plates

	$Re_D \times 10^{-5}$	3.99	5.98	7.97	9.97
FP	Drag Force (N)	91.3	195.9	338.6	510.3
	$C_D \times 10^3$	4.740	4.520	4.395	4.239
DD1	Drag Force (N)	97.0	207.8	356.3	534.0
	$C_D \times 10^3$	5.036	4.794	4.624	4.436
	ΔC_D%	6.3	6.1	5.2	4.7
DD2	Drag Force (N)	94.0	201.5	347.3	519.3
	$C_D \times 10^3$	4.881	4.650	4.507	4.314
	ΔC_D%	2.97	2.88	2.56	1.8
DD3	Drag Force (N)	89.8	189.5	309.5	432.0
	$C_D \times 10^3$	4.660	4.373	4.017	3.589
	ΔC_D%	-1.7	-3.3	-8.6	-15.3
DD4	Drag Force (N)	90.3	192.5	330.3	487.3
	$C_D \times 10^3$	4.686	4.442	4.287	4.048
	ΔC_D%	-1.1	-1.7	-2.5	-4.5

Figure 8 provides an overview of the drag reduction potential of the dimpled surfaces across different boundary layer thicknesses. For the thin boundary layer condition (BL0), characterized by a boundary layer thickness to dimple diameter ratio (δ/D) ranging from 0.115 to 0.130 at the leading edge and an average of 0.215 to 0.240, the data suggest that each dimple configuration (f_a value) has a specific Reynolds number (Re_D) interval in which drag reduction is the most effective. Outside of this optimal interval, both lower and higher Re_D values result in increased drag coefficients due to the dimpled surface implementation.

As the f_a value decreases from DD1 to DD4, the effective Re_D interval for the drag reduction shifts to higher values, with increasing effectiveness in drag coefficient reduction. For instance, DD2 begins to show an optimal drag reduction at slightly lower Re_D values, achieving a 3.0% reduction in drag coefficient at $Re_D \approx 4 \times 10^5$. This reduction peaks at 4.1% at $Re_D \approx 8 \times 10^5$ before decreasing to 2.5% at $Re_D \approx 1 \times 10^6$. DD3 exhibits significant potential, with the effective interval starting at around $Re_D \approx 4 \times 10^5$, achieving a 2.3%

reduction in the drag coefficient and approaching an outstanding reduction rate of 17.1% at $Re_D \approx 1 \times 10^6$, possibly reaching its maximum effectiveness at slightly higher Re_D values. DD4, with a sparser pattern, displays a similar trend in drag coefficient reduction but at lower rates compared to DD3. This suggests that the tested Re_D range may only represent the initial part of DD4's optimal interval. We anticipate that DD4 might achieve higher drag reduction rates within the range of $1.3 \times 10^6 < Re_D < 1.7 \times 10^6$. Conversely, DD1 shows a modest drag reduction at lower Re_D values but exhibits an increasing trend of additional drag force, peaking at a 4.7% increase in the drag coefficient at $Re_D \approx 1 \times 10^6$. Therefore, it is inferred that the optimal Re_D interval for DD1 is likely lower than the range examined in this study.

Under the condition of a larger boundary layer thickness (BL1), where the boundary layer to dimple diameter ratio (δ/D) ranges from 0.290 to 0.238 at the leading edge and from approximately 0.215 to 0.240 on average, it can be observed that dimpled surfaces generally experienced higher drag resistance compared to those with thinner boundary layers. However, the effects of an increased boundary layer thickness on dimpled surfaces differ depending on the f_a ratios.

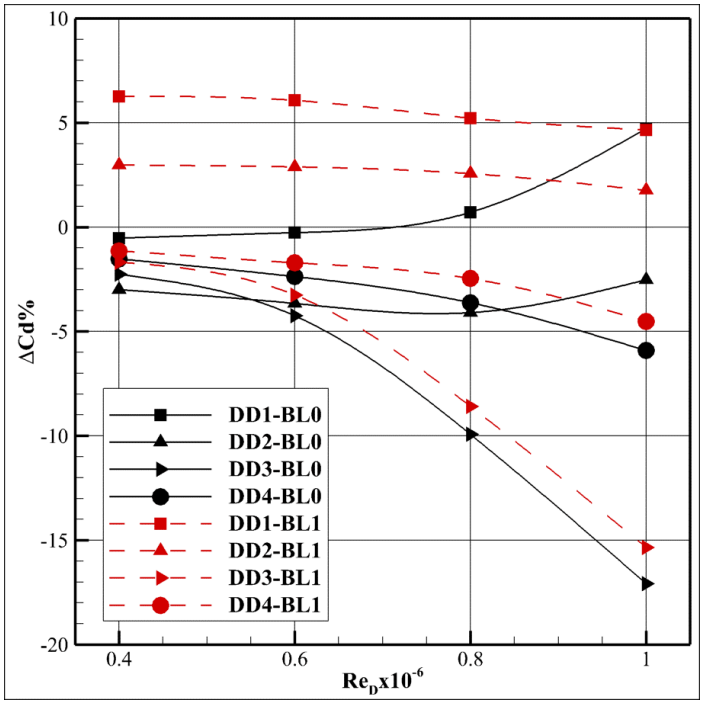

Fig. 8 Difference in the drag coefficient percentages of the dimpled surfaces compared to the flat plate

When analyzing the DD3 and DD4 data, it can be observed that the reduction in the drag coefficient was less for BL0 compared to BL1. Additionally, the variation in the drag coefficient difference with the increase in velocity (Re_D) shows characteristics similar to those under condition BL0 compared to the flat plate. However, DD1 and DD2 were significantly affected by the increase in the boundary layer thickness, exhibiting a different drag coefficient variation with an increase in velocity compared to those under condition BL0. For instance, at $Re_D \approx$ 4x10^5, under condition BL0, DD1 yielded a drag reduction of ~0.5% compared to the flat plate (FP), whereas under condition BL1, with the reverse behavior increasing the drag coefficient by 6.3%. However, as the incoming flow velocity increases, this value decreases and approaches that under condition BL0, falling to a drag augmentation of 4.7% at $Re_D \approx$ 1x10^6. A similar trend was observed for DD2, which shows a decreasing drag coefficient curve as the Re increases. Analyzing the thick boundary layer (BL1) results alone, a decrease in the drag coefficients can be observed for all of the dimpled plates compared to the flat plate, as the incoming flow velocity increased. This observation likely indicates a change in the dominant flow mechanism under BL1 conditions compared to BL0.

According to previous studies in the literature, the frictional drag-reduction mechanisms of the dimpled structures generally fall into two categories. The first involves changes in the boundary-layer velocity profile within the dimpled structure and a reduction in the average shear stress magnitude in the flow direction on the

surface. Additionally, these structures can enhance the form drag. These effects primarily result from the formation of low-pressure regions due to flow separation at the leading edge, if present, and the expansion–contraction effect, which generates additional shear stresses in the regions between dimples due to local accelerations near the dimple edges and increases the pressure from impact effects in the upstream flow region. The second drag-reducing mechanism involves the induction of spanwise velocity perpendicular to the flow and parallel to the surface, with the intensity of this induction increasing based on the arrangement of the dimples, thereby passively inducing oscillatory wall effects. References [22-24, 30, 31] provide detailed explanations of these effects under the conditions they were studied.

The first mechanism is considered to be dependent on the incoming velocity and, as discussed in [30], on the change rate of the cross-sectional area of the dimpled structure and the boundary layer momentum thickness. The fundamental principle here is the trajectory and vertical extension of the viscous sublayer region and the logarithmic layer where the momentum generally increases within the dimpled structure. This is because a standard boundary layer characteristic is not observable within the dimpled structure, and the velocity profile in the flow direction does not resemble that of a standard turbulent boundary layer. Moreover, the rule that the pressure gradient normal to the surface within the boundary layer remains close to zero also changes. In this context, the desired viscous sublayer stretching and, thus, the reduction in the *du/dy* gradient on the surface, is critical for reducing frictional drag. However, this should occur without flow separation. When flow separation does occur, frictional drag can yield negative values in that region, and although an increase in pressure is generally expected because of the lower velocities, the nature of flow separation creates a low-pressure region, which significantly increases the form drag. Additionally, even in the absence of flow separation, if the boundary layer stretching is significant at the lower sections, the high-momentum streak in the logarithmic and outer boundary layer regions advances with a smaller gradient than the geometric inclination of the dimpled structure, causing the flow lines in this streak to approach the downstream edge of the dimple more perpendicularly, having an impact with an increase in the pressure in this region. This also contributes to increased form drag. This is schematically illustrated in the hypothetical drawings shown in Figure 9. The critical point here is to determine the optimal relationship between the velocity and dimpled structure geometry that minimizes the total drag by sacrificing a certain amount of the reduction in frictional drag while maintaining form drag at a reasonable level.

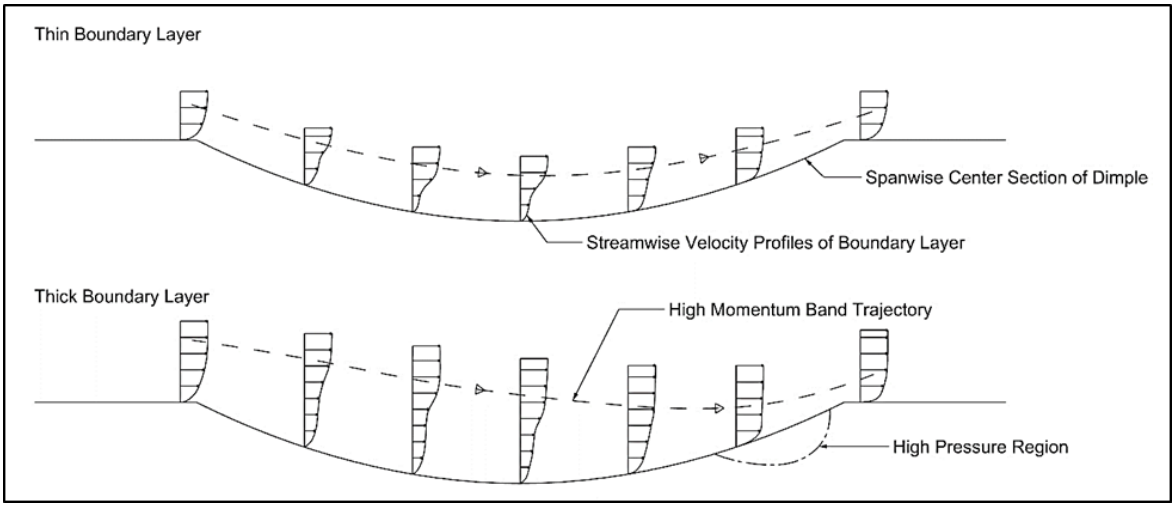

Fig. 9 Hypothetical visualization of thin and thick streamwise boundary layer profiles propagating through the spanwise center plane of the dimples

The second mechanism is actually the primary means of drag reduction. This mechanism involves the passive induction of spanwise flow. An important aspect of this phenomenon is that the arrangement of dimples relative to each other creates effective transverse flows due to the interactions among them. The location, direction, and severity of these transverse flows are also crucial. These interactions occur particularly in regions near the surface where the flow enters and exits the dimple structure. Instead of following a single strip along the spanwise centerline of the dimpled structure, the flow progresses toward the lateral edges and

forms angles of approximately 20-30 degrees with the general flow direction. As a result, the components of the wall shear stress that contribute to drag in the flow direction are reduced.

Supported by previous literature [21, 23, 25, 27, 29, 42], the hypothetically created Figure 10, attempts to explain the possible induced velocity magnitudes and streaklines on a plane parallel to the flat surfaces among dimples at a distance that remains within the boundary layer. In the figure, HCR, MCR, and LCR are abbreviations for high-, medium-, and low-coverage ratios (f_a), respectively. The colored circles represent the relative magnitudes of local average flow velocities compared to the average velocity of the flat plate. Red "H" indicates high, green "A" denotes approximately the same, and blue "L" signifies low.

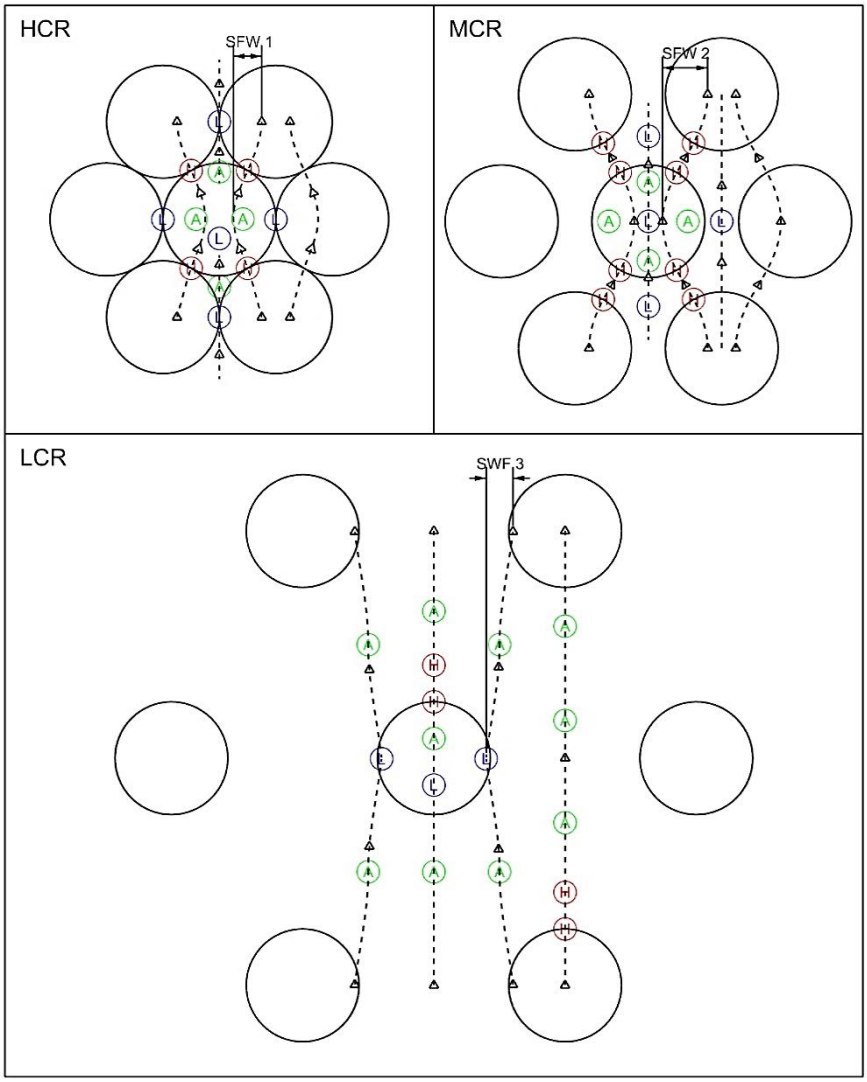

Fig. 10 Depictions of hypothetical streaklines which represent flow regimes induced by different dimple arrangements based on the coverage ratio

In the figure, HCR and MCR illustrate scenarios in which the flow speed close to the wall is optimal. LCR, on the other hand, represents a situation where the dimple arrangement is very sparse, leading to insufficient interaction among the dimples. In the HCR arrangement, if the flow velocity exceeds the ideal level, vortices aligned with the spanwise direction, which induce spanwise flow among dimples, are stretched and their effective diameters are reduced. As a result, while velocity fluctuations increase, the distance denoted as SWF1 decreases. Consequently, although the dimples are closer to each other, the flow patterns resemble those depicted in LCR, but with an additional increase in the velocity of the flow lines moving along the general flow direction over the spanwise centerline of the dimpled structure.

Regarding the ideal velocity conditions, two key factors contributing to drag reduction can be identified. First, in the regions between consecutive dimpled structures oriented spanwise, the magnitude of the wall-normal flow velocity is lower compared to a flat plate. This suggests that frictional drag is reduced compared to the flat plate in these regions. Second, in the regions between two diagonal dimples, where the average velocity magnitudes and velocity gradients are high, the angles of the flow lines relative to the general flow direction and the amplitude of the sinusoidal wave pattern of these flow lines indicate the extent to which the wall shear stress component in the flow direction decreases and the spanwise shear stress component increases.

Based on these assessments, several hypotheses can be made upon re-evaluating the drag data obtained in our study. DD1, even at the lowest speed tested under condition BL0, contains the primary mechanism depicted in the upper part of Figure 9. Thus, despite the increase in velocity and the corresponding thinner boundary layer, there is no significant reduction in the form drag. Furthermore, the positive effects of the spanwise flow induction, as previously described, diminish with an increase in the velocity due to the reduced amplitude of SWF1 relative to the current arrangement density. Consequently, some form drag persists, which generally increases the total drag. When the boundary layer thickness increases to BL1, a significant event occurs, as depicted in the lower part of Figure 9, which substantially increases the form drag due to the reduced flow velocity magnitudes near the wall surface. As the incoming flow velocity increases, the form drag decreases because the internal flow within the dimpled structure approaches the state indicated in the upper part of the figure. Nevertheless, at high speeds, the lower velocity magnitudes at a certain distance perpendicular to the surface in BL1 compared to BL0 result in a smaller excess of the spanwise flow component according to the arrangement density.

For DD2, under condition BL0 at $Re_D \approx 8\text{x}10^5$, it likely operates in the most efficient state as illustrated in the upper right part of Figure 10, achieving its maximum drag-reduction capacity under the examined conditions. Under condition BL1, DD2 is presumably in a situation similar to DD1, as previously explained. The reason why the increase in the boundary layer thickness does not have such a detrimental effect for DD3 and DD4 could be the higher number of dimpled structures in DD1 and DD2 compared to DD3 and DD4. The negative effects of the primary mechanism are less pronounced when the number of dimpled structures decreases. Regarding the secondary mechanism, a greater distance between dimples allows vortices inducing spanwise flow to have larger diameters. Thus, even though the velocity magnitudes near the surface decrease with the increase in the boundary layer thickness, the vortices still extend to the outer regions of the boundary layer and retain their significant effects. Consequently, condition BL1 still causes a slight reduction in performance for both DD3 and DD4 compared to condition BL0.

In summary, a near-certain requirement is that, under existing flow conditions, no flow separation occurs within the dimples, and form drag is kept as low as possible. The depth ratio of the dimpled structure and the slopes at the leading and trailing edges are crucial in this regard. The ideal density of the dimple placement (f_a ratio) may vary depending on the flow conditions. This ratio is influenced not only by Re_D but also by the boundary layer thickness and the characteristics of the velocity profile within the boundary layer, particularly affecting the velocity magnitudes and gradients in the wall-normal region. Thus, channel flows with an inherently constrained boundary layer thickness may yield different results compared to external flow conditions. However, it is important to note that the comments made here are based on the obtained drag results and previous literature and are presented as hypotheses.

5. Conclusion

An experimental study was conducted in the large cavitation tunnel of Istanbul Technical University using a specifically designed setup with large testing plates to assess the resistance reduction characteristics of circular dimple structures under high freestream velocities and varying boundary layer thicknesses, conditions that are rarely addressed in the literature. Based on the obtained resistance values and analyses utilizing previous studies, the following conclusions were drawn:

- Based on the experiments conducted, it was observed that under high-speed external flow conditions representative of real-life scenarios, dimpled structures can be highly effective in reducing frictional resistance, provided certain conditions are met within the required specific ranges. The most promising

result obtained from the experiments was achieved under conditions of $Re_D = 1x10^6$, $\delta/D \approx 0.115$, and $f_a = 0.537$, which led to a 17.1% reduction in resistance compared to that of the flat plate.

- There is no ideal value for the coverage ratio of the dimple arrangements under all conditions. Generally, as the external flow velocity increases, the coverage ratio (f_a) decreases. While it is quite challenging to make definitive judgments, based on the values obtained, the optimal f_a value in the range of $8x10^5 < Re_D < 1.2x10^6$ is between 0.3 and 0.6. However, because it significantly alters the velocity magnitudes in the vicinity of the surface, the boundary layer thickness and the velocity profile changes within the boundary layer also have a considerable impact. Although it can be said that efficiency generally decreases with an increasing boundary layer thickness, further detailed studies are needed in this regard.
- It is believed that there are two fundamental mechanisms determining the efficiency of the system. One mechanism depends on the variation in the streamwise velocity profile within the dimple, where the geometric characteristics of the dimple structure in relation to the external flow conditions are crucial. The other mechanism is related to the lateral velocity induction capacity of the dimple structures, which affects the reduction in streamwise friction resistance by altering the direction of turbulent kinetic energy and shear stresses, and it is significantly influenced by the coverage ratio (f_a) of the dimple structures. Although these two factors interact somewhat based on Re_D and the boundary layer characteristics of the overall flow, they generally affect independently and provide efficiency values that could be meaningful within an optimal range that is difficult to estimate.
- The entrance and exit slopes, the cross-sectional expansion ratio of the dimple structure, and the flow speed and boundary layer characteristics of the flow are factors that affect the drag-reduction capability of dimple applications. Further research on different types of dimples (elliptical, diamond, etc.) that investigates the effects of a high Reynolds number, coverage ratio, and boundary layer thickness ratio may reveal more beneficial flow patterns.
- Although notable resistance reductions have been observed under certain conditions, these reductions occur in very specific situations. Therefore, the practical applicability of these results is arguable in scenarios in which external flow conditions can vary significantly. For instance, in commercial vessels, in areas with flat bottoms and parallel hulls that are suitable for dimple applications, the boundary layer thickness will vary, potentially requiring changes in the f_a ratio from fore to aft. This implies that a thorough research process is needed for each specific vessel. Additionally, the system to be implemented should naturally align with the cruising speed. That is, the arrangement of the dimple structures applied for cruising speed is likely to increase resistance rather than reduce it at lower speeds.
- If dimples are to be implemented on a ship, they should primarily be positioned on the parallel hull and flat base surface of the ship, if available. However, that the thickness of the boundary layer increases as one progresses from the bow to the stern of a ship, it is considered that to maximize the resistance reduction, the coverage ratio (f_a) should be adjusted. Although it is generally anticipated that the decrease in the coverage ratio will have a positive effect on the drag reduction, when the distance between the dimples does not allow for an interaction inducing spanwise velocities, the reduction in drag may be diminished. Therefore, instead, increasing the diameter of the dimples while keeping their depth constant might be a more appropriate application. However, a more reliable conclusion on this matter could be reached following detailed studies to be conducted in the future.
- Another issue is the lack of information regarding how sensitive the performance of the dimple structure arrangement is to changes in the incoming flow direction. Particularly for marine vehicles, the wave patterns generated by the vehicle's own hull, as well as the variable flow conditions due to currents and wave propagations in rough weather and sea conditions, might have significant adverse effects. On the other hand, dimples may have an even greater advantage for marine crafts with a small water-plane area to displacement ratio, such as SWATH ships or semi-submersibles, and for fully submerged vehicles, such as submarines or torpedoes, which have none or a very small wave-making drag component and low degree of interaction with sea surface conditions. Further research is needed in this area.

This study emphasizes the significant potential of dimpled structures in reducing frictional resistance and provides valuable insights and experimental data in a range of high Reynolds numbers, which is critical for practical engineering applications. Our findings suggest that while dimple structures are, indeed, suitable for rail transport where the external flow conditions are somewhat stable, the complex conditions in maritime transport require more thorough research for their design in specific marine vehicles.

ACKNOWLEDGEMENT

The experimental work was supported by the Scientific Research Projects Coordination Unit of Istanbul Technical University (ID: MGA-2022-43718).

Special thanks are extended to ITUKAT technicians Seyfi Erim, Mustafa Yalçınkaya and Selçuk Erim, for their efforts during the tests.

NOMENCLATURE

BL	boundary layer
CFD	computational fluid dynamics
EFD	experimental fluid dynamics
FP	flat plate
RANS	Reynolds averaged Navier–Stokes
SST	shear-stress transport
C_D	drag force coefficient
C_F	frictional force coefficient
D	diameter of dimple
d	depth of dimple
f_a	coverage ratio
H	height of flow channel
k	turbulence kinetic energy
$L_{C\text{-}C}$	distance between dimple centers
Re_D	Reynolds number based on diameter
Re_δ	Reynolds number based on δ
V_∞	free-stream flow velocity
y^+	non-dimensional wall distance
δ	boundary layer thickness
ν	kinematic viscosity
ω	specific rate of dissipation

REFERENCES

[1] Tanaka, T., Oishi, Y., Park, H.J., Tasaka, Y., Murai, Y., Kawakita, C., 2021. Repetitive bubble injection promoting frictional drag reduction in high-speed horizontal turbulent channel flows. *Ocean Engineering*, 239, 109909. https://doi.org/10.1016/j.oceaneng.2021.109909

[2] Wang, H., Wang, K., Liu, G., 2022. Drag reduction by gas lubrication with bubbles. *Ocean Engineering*, 258, 111833. https://doi.org/10.1016/j.oceaneng.2022.111833

[3] Zhao, X., Zong, Z., 2022. Experimental and numerical studies on the air-injection drag reduction of the ship model. *Ocean Engineering*, 251, 111032. https://doi.org/10.1016/j.oceaneng.2022.111032

[4] Lyu, X., Tang, H., Sun, J., Wu, X., Chen, X., 2014. Simulation of microbubble resistance reduction on a suboff model. *Brodogradnja*, 65(2), pp. 23-32.

[5] Choi, H., Yoon, H., 2016 Research on hull-form optimization of a passenger ship using hull-form modification algorithm with Gaussian distribution function. *Brodogradnja*, 67(3), pp. 1-15. https://doi.org/10.21278/brod67301

[6] Solak, H.P., 2020. Multi-dimensional surrogate based aft form optimization of ships using high fidelity solvers. *Brodogradnja*, 71(1), pp. 85-100. https://doi.org/10.21278/brod71106

[7] Gruneberger, R. and Hage, W., 2011. Drag characteristics of longitudinal and transverse riblets at low dimensionless spacings. *Experiments in Fluids*, 50(2), pp. 363–373. https://doi.org/10.1007/s00348-010-0936-7

[8] Viswanath, P.R., 2002. Aircraft viscous drag reduction using riblets. *Progress in Aerospace Sciences*, 38(6-7), pp. 571–600. https://doi.org/10.1016/S0376-0421(02)00048-9

[9] Mai, T.D, Kim, S., Chang, K., Lee, S., Kim, M., Ryu, J., 2022. Numerical and theoretical analysis of the influences of surface treatment on drag reduction in submarine. *Ocean Engineering*, 266(4), 113068. https://doi.org/10.1016/j.oceaneng.2022.113068

[10] Kim, S., Chang, K., Lee, S., Kim, M., Yoon, J., J Ryu, J., 2024. Numerical study of hydrodynamic drag effects of streamwise riblet structures on SUBOFF bare hull model. *Ocean Engineering*, 310(2), 118783. https://doi.org/10.1016/j.oceaneng.2024.118783

[11] Dean, B., Bhushan, B., 2010. Shark-skin surfaces for fluid-drag reduction in turbulent flow: a review. *Philosophical Transactions of the Royal Society A*, 368(1929), pp. 4775–4806. https://doi.org/10.1098/rsta.2010.0201

[12] Afanasyev, V.N., Chudnovsky, Y.P., Leontiev, A.I., Roganov, P.S., 1993. Turbulent flow friction and heat transfer characteristics for spherical cavities on a flat plate. *Experimental Thermal and Fluid Science* 7(1), pp. 1–8. https://doi.org/10.1016/0894-1777(93)90075-T

[13] Mahmood, G.I., Ligrani, P.M., 2002. Heat transfer in a dimpled channel: combined influences of aspect ratio, temperature ratio, Reynolds number, and flow structure. *International Journal of Heat and Mass Transfer*, 45(10), pp. 2011-2020. https://doi.org/10.1016/S0017-9310(01)00314-3

[14] Iuso, G., Onorato, M., Spazzini, P.G., Di Cicca, G.M., 2002.Wall turbulence manipulation by large-scale streamwise vortices. *Journal of Fluid Mechanics*, 473, pp. 23-58. https://doi.org/10.1017/S0022112002002574

[15] Choi J.I., Xu C.X, Sung H.J., 2002. Drag reduction by spanwise wall oscillation in wall-bounded turbulent flows. *AIAA Journal*, 40(5), pp. 842–850. https://doi.org/10.2514/2.1750

[16] Yakeno, A., Hasegawa, Y., Kasagi, N., 2014. Modification of quasi-streamwise vortical structure in a drag-reduced turbulent channel flow with spanwise wall oscillation. *Physics of Fluids*. 26(8), pp. 85–109. https://doi.org/10.1063/1.4893903

[17] Quadrio, M., Ricco, P., 2004. Critical assessment of turbulent drag reduction through spanwise wall oscillations. *Journal of Fluid Mechanics*, 521, pp. 251–271. https://doi.org/10.1017/S0022112004001855

[18] Du Y., Symeonidis V., Karniadakis G.E., 2002. Drag reduction in wall bounded turbulence via a transverse travelling wave. *Journal of Fluid Mechanics*, 457, pp. 1-34. https://doi.org/10.1017/S0022112001007613

[19] Zhao, J., Chew, Y., Khoo, B., 2004. Experimental studies on hydrodynamic resistance and flow pattern of a narrow flow channel with dimples on the wall. In: *The American society of Mechanical Engineers*, 2004 international mechanical engineering congress and exposition. https://doi.org/10.1115/IMECE2004-59506

[20] Wüst, C., 2004. Dellen im Dach. Der Spiegel, pp. 170–172. http://magazin.spiegel. de/EpubDelivery/spiegel/pdf/30346859

[21] Lienhart, H., Breuer, M., Köksoy, C., 2008. Drag reduction by dimples? – a complementary experimental/numerical investigation. *International Journal of Heat and Fluid Flow*, 29(3), pp. 783–791. https://doi.org/10.1016/j.ijheatfluidflow.2008.02.001

[22] Veldhuis, L.L.M., Vervoort, E., 2009. Drag effect of a dented surface in a turbulent flow. In: Collection of Technical Papers - *AIAA Applied Aerodynamics Conference* 27. https://doi.org/10.2514/6.2009-3950

[23] Tay, C.M.J., Khoo, B.C., Chew, Y.T., 2015. Mechanics of drag reduction by shallow dimples in channel flow. *Physics of Fluids* 27(3), 035109. https://doi.org/10.1063/1.4915069

[24] Van Nesselrooij, M., Veldhuis, L.L.M., van Oudheusden, B.W., Schrijer, F.F.J., 2016. Drag reduction by means of dimpled surfaces in turbulent boundary layers. *Experiments in Fluids*, 57(9), 142. https://doi.org/10.1007/s00348-016-2230-9

[25] Spalart, P.R., Shur, M., Strelets, M., Travin, A., Paschal, K.B., Wilkinson, S.P., 2019. Experimental and numerical study of the turbulent boundary layer over shallow dimples. *International Journal of Heat and Fluid Flow*, 78, 108438. https://doi.org/10.1016/j.ijheatfluidflow.2019.108438

[26] Van Campenhout, O.W.G., van Nesselrooij, M, Lin Y.Y, Casacuberta, J., van Oudheusden, B.W., Hicke, S., 2023. Experimental and numerical investigation into the drag performance of dimpled surfaces in a turbulent boundary layer. *International Journal of Heat and Fluid Flow*, 100, 109110. https://doi.org/10.1016/j.ijheatfluidflow.2023.109110

[27] Tay, C.M.J., Khoo, B.C., Chew, Y.T., 2017. Use of DES in mildly separated internal flow: dimples in a turbulent channel. *Journal of Turbulence*, 18(12), pp. 1180–1203. https://doi.org/10.1080/14685248.2017.1368528

[28] Ng, J.H., Jaiman, R.K., Lim, T.T., Tay, C.M., Khoo, B.C., 2020. Geometric effects of shallow dimples in turbulent channel flows at $Re_\tau \approx 180$: a vorticity transport perspective. *Flow, Turbulence and Combustion*. pp. 1–40. https://doi.org/10.1007/s10494-020-00112-6

[29] Eng, Y., Tay, C.M.J., Khoo, B.C., 2023. Drag and heat transfer in turbulent channel flow over shallow circular dimples: The shift of the deepest point of dimples. *International Journal of Thermal Sciences*, 185, 108049. https://doi.org/10.1016/j.ijthermalsci.2022.108049

[30] Ilter, Y.K., Çetinkaya, A., Ünal, U.O., 2023. Large eddy simulations of the turbulent channel flow over dimpled surfaces. *Journal of Turbulence*, 24(3–4). https://doi.org/10.1080/14685248.2023.2186415

[31] İlter, Y.K, Ünal, U.O., Shi, W., Tokgöz, S., Atlar,M., 2024. An experimental investigation into the drag reduction performance of dimpled plates in a fully turbulent channel flow. *Ocean Engineering*, 307, 118198. https://doi.org/10.1016/j.oceaneng.2024.118198

[32] Wu, J., Yeo, K.S., 2011. Flow past dimpled surfaces; Part 2: computational study for turbulent flow in dimpled channels. In: *Annual Report on the NUS-Airbus Collaboration under Project R*-265-000-272, 597.

[33] Erbas, B., 2019. The turbulent boundary layer and frictional drag characteristics of new generation marine fouling control coatings. *Brodogradnja*, 70(4), pp. 51-65. https://doi.org/10.21278/brod70404

[34] Hama, F., 1954. Boundary-layer characteristics for smooth and rough surfaces. *Transactions- The Society of Naval Architects and Marine Engineers* 62, pp. 333–358.

[35] Menter, F.R., 1994. Two-equation eddy-viscosity turbulence models for engineering applications. *AIAA Journal*, 32(8), pp. 1598–1605. https://doi.org/10.2514/3.12149

[36] Tennekes, H., Lumley, J.L., 1972. A First Course in Turbulence. *MIT Press*, Cambridge, UK. https://doi.org/10.7551/mitpress/3014.001.0001

[37] Blazek, J., 2001. Computational Fluid Dynamics: Principles and Applications. *Elsevier*, Oxford, UK.

[38] Versteeg, H.K., Malalasekera, W., 2007. An Introduction to Computational Fluid Dynamics, 2nd Edition. *Pearson Education Limited*, Essex, England.

[39] Patankar, S.V., Spalding, D.B., 1972. A calculation procedure for heat, mass and momentum transfer in three-dimensional parabolic flows. *International Journal of Heat and Mass Transfer*, 15, pp. 1787–1806. https://doi.org/10.1016/0017-9310(72)90054-3

[40] Pletcher, R.H., Tannehill, J.C., Anderson, D.A., 2013. Computational Fluid Mechanics and Heat Transfer, 3rd Edition. *CRC Press*, Florida, USA.

[41] Celik, I.B., Ghia, U., Roache, P.J., Freitas, C.J., Coleman, H., Raad, P.E., 2008. Procedure for estimation and reporting of uncertainty due to discretization in CFD applications. *Journal of Fluids Engineering – Transactions of ASME*. 130(7), pp. 1–4. https://doi.org/10.1115/1.2960953

[42] Nasr, M.A., Tay, C.M., Khoo, B.C., 2023. The thermo-aerodynamic performance of turbulent channel flow over dimples of different sizes. *Physics of Fluids*, 35, 075131. https://doi.org/10.1063/5.0155806